The Astrophysical Journal, 604:924–935, 2004 April 1

CHARACTERISTIC SCALES OF CHROMOSPHERIC OSCILLATION WAVE PACKETS

Scott W. McIntosh
Universities Space Research Association, Cooperative Program in Space Sciences, Seabrook, MD 20706; and Laboratory for Astronomy and Solar Physics, NASA Goddard Space Flight Center, Code 682.3, Greenbelt, MD 20771; scott@grace.nascom.nasa.gov

and

Darren G. Smillie[1]
Laboratory for Astronomy and Solar Physics, NASA Goddard Space Flight Center, Code 682.3, Greenbelt, MD 20771; darren.smillie@imperial.ac.uk
Received 2003 September 3; accepted 2003 December 17

ABSTRACT

We use wavelet transforms to study the characteristic time scales of chromospheric oscillation "wave packets" that are observed in *Transition Region and Coronal Explorer* (*TRACE*) ultraviolet continuum image time series. Using several data sets, we investigate the statistical, spatial, and temporal intermittence of the number, duration, mean frequency, and delay ("wait time") between wave packets in the time series data. Further, we demonstrate that these characteristic values are consistent with newly developed pictures of the wave-mode suppression and conversion by the chromospheric magnetic "canopy." We propose that wavelet analysis may be fruitfully used in diagnosing the structure of the chromosphere and in identifying chromospheric oscillation wave packets temporally and spatially with their photospheric sources.

Subject headings: Sun: atmospheric motions — Sun: chromosphere — Sun: magnetic fields — Sun: transition region — Sun: UV radiation

On-line material: color figures

1. INTRODUCTION

Oscillations observed in the upper photosphere, chromosphere, and transition region plasmas have been noted to interact symbiotically with the atmospheric plasma topography[2] in which they are observed (see, e.g., McIntosh et al. 2001; Krijger et al. 2001; McIntosh & Judge 2001; McIntosh, Fleck, & Judge 2003 and references therein). These oscillations are generally acoustic in nature, stem from either the global *p*-modes that propagate in the Sun's interior (Ulrich 1970) through superposition and interference, producing an apparently random wave field (White & Cha 1973; Cha & White 1973), or the thermodynamic collapse of granular cells (Rast 1999; Skartlien & Rast 2000), and have received considerable attention as one possible source of energy and support for the ambient quiet chromosphere and corona (see the excellent review of Rutten 2003). They manifest themselves in the Sun's outer atmosphere as small, isolated, but systematic "packets" of as few as one, two, or three wave periods that lose coherence or switch off and wait for a measurable amount of time before the next packet occurs. We primarily focus on the analysis of these "wave packets"[3] in the chromosphere, where they are simply dubbed chromospheric oscillations.

To date, much of the analysis performed on chromospheric oscillations has been based on Fourier techniques, which, more or less by definition, assume that the observed wave modes are persistent spatially and temporally over the duration of the observation. Significant insight into the nature and propagation of chromospheric oscillations has been provided by Fourier analysis (see, e.g., Rhodes, Ulrich, & Deubner 1979; Lites, Chipman, & White 1982; Deubner & Fleck 1990; and most of the papers cited previously). However, the source, or "piston," of chromospheric oscillations dictates the analysis method required; granular collapse and "local" interference of multiple, global *p*-modes are highly intermittent in time and space. In such cases of intermittent excitation, Fourier analysis is inadequate, and we should instead employ a method that can capture the full temporal and spatial dependence of chromospheric oscillations. It is exactly the spatial and temporal intermittence of chromospheric oscillations and their (unresolved) generation mechanism that makes their analysis amenable to a multiscale, time-frequency wavelet transform analysis as a natural extension to the standard (Fourier) frequency domain analysis. Put simply, wavelet transforms allow the localization of the packet in the frequency and time domains simultaneously with a small trade-off in accuracy (see, e.g., Torrence & Compo 1998). In the following sections we discuss the application of wavelet transforms to chromospheric oscillation analysis and explore some of the temporally and spatially local features that result.

In § 2 we discuss the data and reduction methods that we apply to the *Transition Region and Coronal Explorer* (*TRACE*; Handy et al. 1999) UV image time series used in this paper. In § 3 we present and demonstrate the application of wavelet transforms to these data and define the packet "parameters" that we employ to characterize, count, and time the chromospheric packets in eight illustrative *TRACE* data sets. Physical attributes of the chromospheric oscillations (and their sources) are readily attached to the defined packet parameters. In § 4 we tabulate the characteristic features of each of those data sets and present, in § 4.1, examples to

[1] Current Address: Department of Physics, Blackett Laboratory, Imperial College London, London SW7 2BW, UK.

[2] Of course, when we refer to the plasma topography we mean the entire plasma structure, including magnetic field topology (the chromospheric "canopy") and the plasma in which it is threaded.

[3] For the purpose of this paper we define a "wave packet" as a short-duration, multifrequency packet of oscillations in time series observations of the solar chromospheric plasma. For brevity, from this point onward we refer to wave packets simply as packets.

illustrate the spatial distribution of packet parameters. Indeed, to extend this work and to point to future investigations of this kind we present, in § 4.2, an investigation into the vertical nature of the packet parameters in a typical, well-studied, multiwavelength (multiple formation temperature) joint *TRACE* and *Solar and Heliospheric Observatory* (*SOHO*; Fleck, Domingo, & Poland 1995) Joint Observing Program (JOP) 72 data set. To close, in § 6, we discuss these results and place them in context with other chromospheric oscillation investigations of the solar atmosphere that can be pursued in the future (§ 5).

2. DATA AND REDUCTION

To characterize the nature of these packets in the outer solar atmosphere, we perform the wavelet analysis for an archive of time series data from *TRACE* that have co-temporal magnetic topological context provided by the *SOHO* Michelson Doppler Imager (MDI; Scherrer et al. 1995). From 1998 May until 2001 August, there are eight data sets of sufficient duration ($\geq$1 hr) and fixed, short *TRACE* cadence ($\sim$15 s) to perform this study. More often than not, such observations were the result of carefully designed *SOHO* JOPs (more specifically JOPs 26, 40, 72, and 97), using multiple instruments on the *SOHO* spacecraft to complement the *TRACE* observations (see, e.g., Judge, Tarbel, & Wilhelm 2001). This relatively small set of observations represents a wide range of solar plasma topographies, from sunspots to (very quiet) disk center internetwork observations.

We use the data reduction method outlined in § 2 of Krijger et al. (2001) to investigate the time series of the *TRACE* continuum bandpass images. The first step in the analysis of the data involves the co-alignment of the initial *TRACE* image and MDI magnetogram of the time series. Then we form data cubes for the *TRACE* time series, D_λ (x, y, t), with each frame co-aligned with the previous one with subpixel accuracy (see, e.g., McIntosh et al. 2003). This image correlation process ensures that the data cubes are as insensitive as possible to the effects of contamination from cross talk in the signal produced by solar rotation. In the following sections we predominantly limit our discussion to the analysis of *TRACE* 1700 Å image time series because of their relatively high feature contrast and signal-to-noise ratio (T. D. Tarbell 2003, private communication) and because, as we show in § 4.2, the measured packet descriptions are consistent in each of the three *TRACE* continua (1550, 1600, and 1700 Å).

Once the images are co-aligned, we spatially rebin the data cubes into $1'' \times 1''$ (i.e., 2×2 *TRACE* pixels) blocks, ensuring an accurate spatial description of the packet with sufficiently high signal-to-noise ratio to isolate spatially local events without smearing the oscillation excessively. Judge et al. (2001) demonstrated (in § 3.3.3 and in Fig. 7 of their paper) that the spatial coherence length scale observed in various JOP 72 *TRACE* chromospheric oscillations studies was of the order of $1''$.

3. MORLET WAVELET ANALYSIS

Figure 1 illustrates the key features and measures used in this paper to characterize packets in the *TRACE* 1700 Å continuum time series observations following the application of the Morlet[4] wavelet transform discussed in Torrence & Compo (1998). This characterization defines when packets statistically exist in a time series, how many packets there are over the duration of the time series, how long they last, how much time passes between packets, and what the mean frequencies of the packet oscillations are. The position of the white asterisk in the top right thumbnail of the *TRACE* field of view (FOV) marks the location of the pixel time series that is presented as an example in Figure 1*a*. At first glance, the time series would appear to present a regular oscillation with a period of about 4 minutes, but the signal seems to be temporally intermittent, with sizeable breaks from regular periodic oscillation.

In Figure 1*b* we show the wavelet power spectrum of this pixel time series, and the regions of high wavelet power are clearly visible. We also show the "cone of influence" (*cross-hatched area under the curve*), which marks the region of uncertainty caused by the finite length of the time series (its shape is a function of the length of the time series and the chosen wavelet basis). Many of the regions of high power have greater than 95% statistical confidence and are placed inside the thick black contours. The power that is contained within each of these closed 95% confidence contours *and* is completely outside the cone of influence defines one instance of the multifrequency packets that we are studying in this paper. When we make the further restriction that we are interested in packet frequencies between 3 and 8 mHz,[5] we can see that there are two "statistically significant" regions of power in this particular hour-long pixel time series.

In Figure 1*c* we show the global wavelet power spectrum (GWPS; Torrence & Compo 1998), which is the mean wavelet power averaged over time and the feature most comparable to the Fourier power spectrum of the time series (except that it is significantly smoother). From the GWPS we are able to define and measure the peak period, 4.13 minutes (frequency of $\sim$4.00 mHz), of the packets present in the 3–8 mHz frequency (5.6–2 minute periodicity) band. Similarly, the GWPS can be integrated over the same range of frequencies to obtain a measure of the average oscillatory power present in that spatial pixel. We note that the lower peak in the GWPS can be neglected, since it belongs to a packet that is predominantly within the cone of influence and is also not statistically significant, each of which is a criterion for rejection.

Figure 1 shows the 3–8 mHz frequency-averaged wavelet power as a function of time. This quantity allows us to measure the time-related parameters of the packets present; the packet duration and the packet "wait time" (the time between packets) along with the peak packet power. The wait time can be thought of as the time between piston actions, or constructive interference events, and the packet duration as the coherent lifetime of the piston, or the coherence time of the impinging *p*-modes. We note that the inclusion of the longer "unfinished" (lighter) packet wait times cause a net underestimation of the mean wait time over the duration of the time series. The dashed line in Figure 1*d* indicates the frequency-averaged 95% confidence level contours of Figure 1*b*; the intersections of this line with the power curve marks the

[4] We note that other wavelet bases are available and may modify the results presented slightly, but the Morlet wavelet best represents the types of sinusoidal oscillations present in our data (see, e.g., O'Shea et al. 2002).

[5] We note that our choice of the wide 3–8 mHz frequency band (including evanescent and propagating wave frequencies in the chromosphere) allows spatial study of packet frequencies with sufficient contrast to identify and evaluate network and internetwork regions in § 4.1; study of smaller, more carefully selected frequency bandpasses is the subject of a future paper (S. W. McIntosh 2004, in preparation).

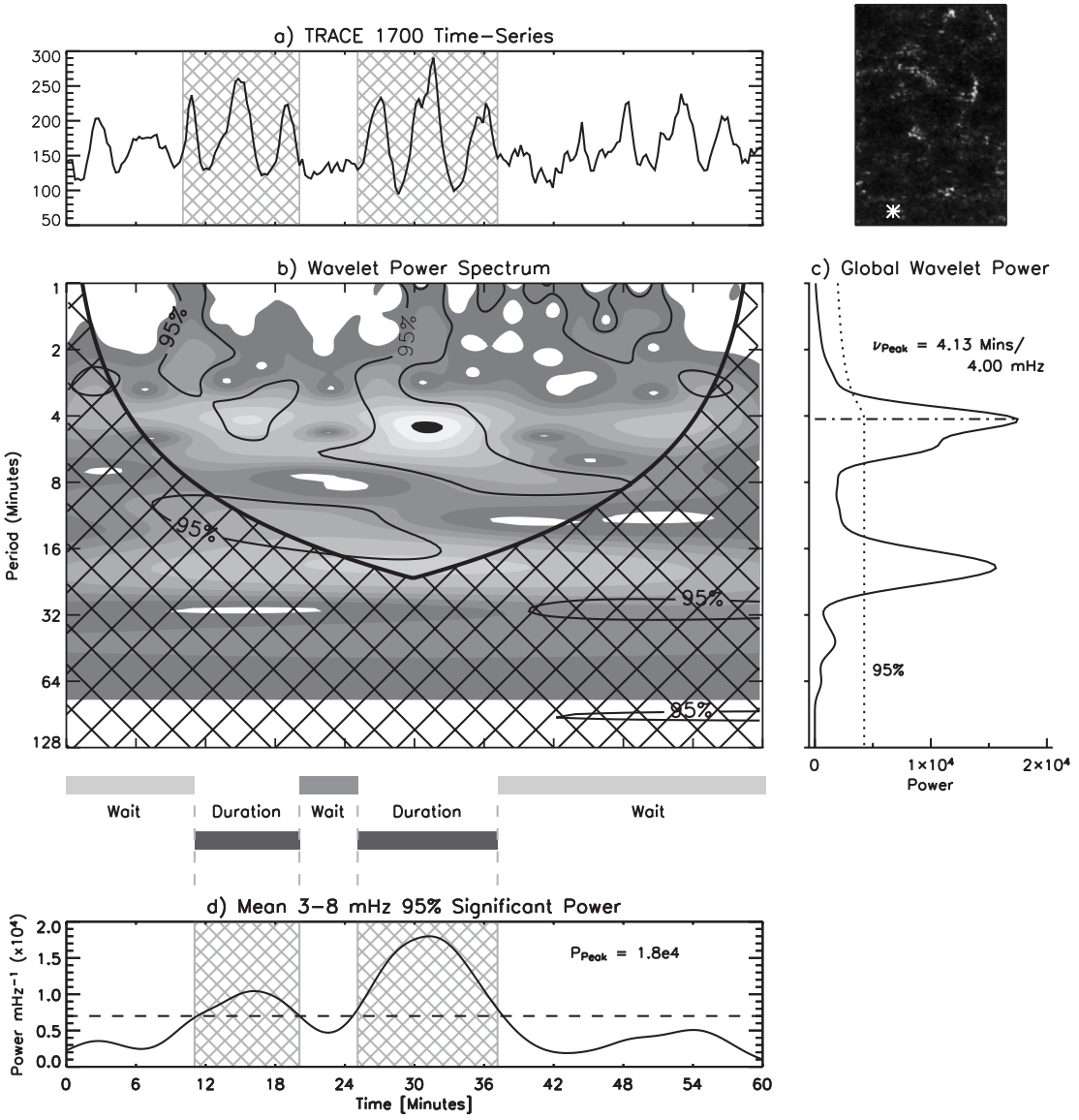

FIG. 1.—Key features and measures used in this paper to characterize chromospheric oscillation wave packets. (*a*) Thumbnail image of the *TRACE* FOV (set 4) and an asterisk marking the location of our sample time series. (*b*) Wavelet power spectrum with 95% confidence inside the black contours. (*c*) GWPS, the mean wavelet power averaged over time, from which we measure the mean packet frequency. (*d*) The 3–8 mHz average of the wavelet power and the average power of the 95% confidence contours. We use the intersection of the latter with the 3–8 mHz average power to mark the temporal boundaries of the packets (*cross-hatched areas*) and consequently define the packet duration and time between packets or the packet "wait time." [*See the electronic edition of the Journal for a color version of this figure*.]

temporal boundaries of the packets. These intersections are marked as finely cross-hatched areas on the panel and are similarly traced onto Figure 1*a*. Visually cross-referencing these cross-hatched regions with the two statistically significant wavelet power regions in Figure 1*b* provides a check for the method.

We have now defined several parameters of the packets present in the 1700 Å *TRACE* continua that we use in the following section, namely, the packet mean frequency ν_X, the packet duration D_X, the packet number N_X, and the packet wait time Δt_X (the subscript X is used to distinguish spatially between the network, $X = N$, and internetwork, $X = I$, regions). To complement these quantities and to normalize for observations of different lengths, we introduce the packet number per hour, $\hat{N}_X$ (indicating the frequency of piston occurrence, or *p*-mode interference), and the number of periods per packet, $\hat{P}_X$ $(= D_X \nu_X)$. We employ these parameters, measured in many time series, to investigate the temporal and spatial characteristics of chromospheric oscillations quantitatively in network and internetwork regions.

4. RESULTS

The packet parameters defined above provide us with a means to characterize chromospheric oscillation time series data temporally, spatially, and statistically. In Figure 2 we present details of the packet parameter histogram samples from the longest time series available, that of the JOP 97 sunspot data, 2000 September 22 (set 7; also discussed in Muglach & Hofmann 2003). At the top of this figure we show, from left to right, the imaging context for the time series in the form of the time-averaged MDI $B_{\|}$ and *TRACE* 1700 Å continuum intensity maps. Between these two images we show the masks that we have defined to delineate the internetwork ("IN"; $|B_{\|}| < 10$ Mx cm^{-2}; *white*), network

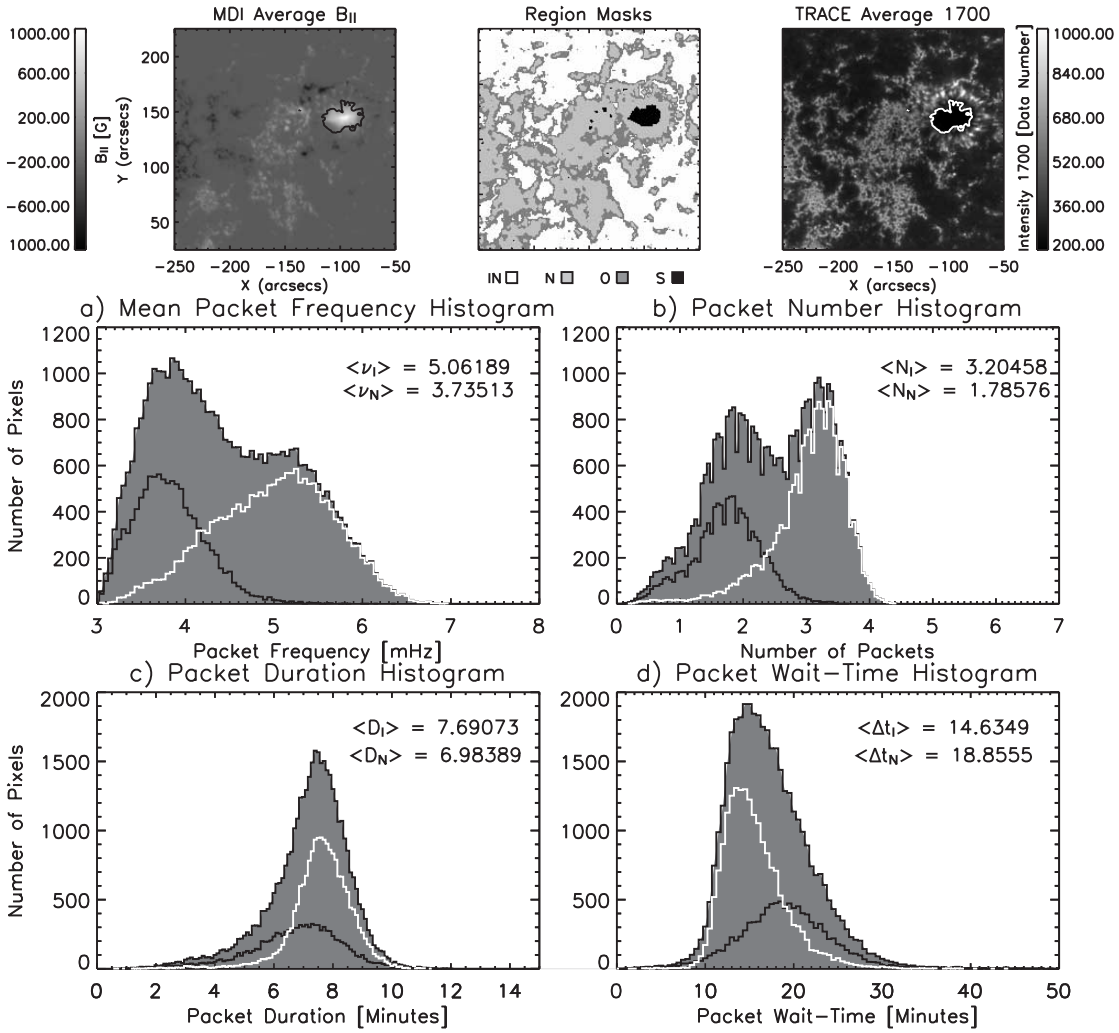

FIG. 2.—Packet parameter histogram samples from the longest frame sequence available, that of the JOP 97 sunspot data, 2000 September 22 (7). At the top of this figure we show, from left to right, the imaging context for the time series in the form of the time-averaged MDI $B_{\|}$ and *TRACE* 1700 Å continuum intensity maps. Between these two we show the various masks that are defined to delineate the internetwork (*white*), network (*gray*), a buffer between them (*dark gray*), and the sunspot (*black*) regions as defined in § 4. In the lower set of panels we present the packet parameter distributions for each of these regions; (*a*) the mean packet frequency ν_X, (*b*) the number of packets N_X, (*c*) the packet duration D_X, and (*d*) the packet wait time Δt_X.

TABLE 1

DETAILS OF THE PACKET DISTRIBUTIONS OBSERVED IN THE EIGHT *TRACE* 1700 Å CONTINUA TIME SERIES DATA SETS STUDIED

Data Set	Date	T_0	n_f	B^*	N_N	$\hat{N}_N$	ν_N	D_N	Δt_N	$\hat{P}_N$	N_I	$\hat{N}_I$	ν_I	D_I	Δt_I	$\hat{P}_I$
1.....	1998 May 12	14:31	353	84.38	2.34	1.59	3.29	9.79	17.21	1.93	3.12	2.12	3.91	10.53	13.76	2.47
2.....	1998 May 16	14:33	345	81.92	2.20	1.53	3.19	9.96	16.23	1.90	3.11	2.16	3.90	10.13	13.19	2.37
3.....	1999 Feb 25	23:05	478	83.82	2.19	1.10	3.21	8.45	18.98	1.87	3.92	1.97	3.95	10.21	14.98	2.42
4.....	1999 Feb 26	23:00	239	16.50	1.81	1.81	3.32	11.49	19.33	2.29	2.36	2.36	3.99	12.08	12.69	2.89
5.....	1999 Sep 11	08:03	444	92.44	2.15	1.16	3.28	8.89	18.84	1.75	3.94	2.12	4.39	9.94	15.83	2.62
6.....	1999 Sep 13	08:02	464	105.65	2.24	1.15	3.34	8.76	19.05	1.76	3.56	1.84	4.25	9.76	16.12	2.49
7.....	2000 Sep 22	08:00	478	162.27	1.78	0.89	3.74	6.98	18.86	1.57	3.20	1.61	5.06	7.69	14.64	2.35
8.....	2001 Aug 17	23:00	430	97.35	1.96	1.09	3.32	8.55	19.56	1.70	3.19	1.78	4.15	9.75	12.99	2.43

NOTES.—Each data set has an index, when the time series commenced, the number of frames in the sequence (n_f) with the time between images in this set fixed ($dt = 15$ s), the mean unsigned network magnetic field strength (B^* in Mx cm^{-2}), and the mean packet parameters of region X discussed in the text (N_X, $\hat{N}_X$, ν_X, D_X, Δt_X, $\hat{P}_X$). The subscript X indicates where the packets were observed; $X = I$ in the internetwork and $X = N$ in network regions.

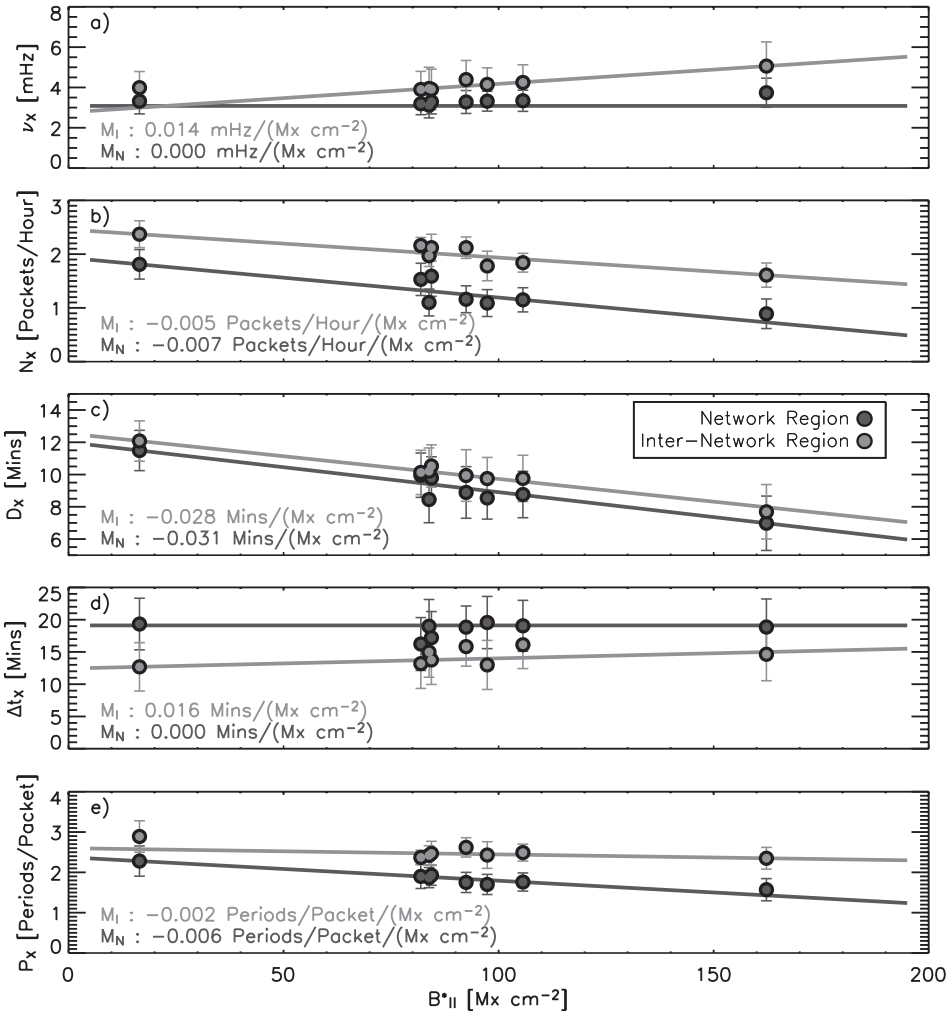

FIG. 3.—(*a*) Packet frequency, ν_X, (*b*) the number of packets per hour, $\hat{N}_X$, (*c*) the packet duration, D_X, (*d*) wait time, Δt_X, and (*e*) number of oscillation periods per packet $\hat{P}_X$ and their variation with the mean unsigned network magnetic field B^*. In each panel we show the network (*dark*) and internetwork (*light*) parameters, their variances, and the best-fit straight line to the points. We also show the network (M_N) and internetwork (M_I) best-fit line gradients. [*See the electronic edition of the Journal for a color version of this figure*.]

("N"; $20 < |B_{\|}| < 400$ Mx cm^{-2}; *light gray*), an intermediate buffer between them ("O"; $10 < |B_{\|}| < 20$ Mx cm^{-2}; *dark gray*) and the sunspot ("S"; $|B_{\|}| > 400$ Mx cm^{-2}; *black*) regions; please note that because of signal-to-noise problems we omit data from the latter (instead see O'Shea, Muglach, & Fleck 2002, who study waves in sunspot umbrae). In the lower set of panels we show the packet parameter distributions for each of these regions: Figure 2*a*, the packet frequency ν_X; Figure 2*b*, the number of packets N_X; Figure 2*c*, the packet duration D_X; and Figure 2*d*, the packet wait time Δt_X. The gray shaded histograms in each panel show the packet parameter distributions for *all* spatial pixels (again, except those of the sunspot). Contained within these shaded histograms are the network (*solid black line*) and internetwork (*solid white line*) parameter distributions that allow us to visualize the spatial differences in the parameters from a statistical standpoint.

Clearly, the all-pixel packet parameter distributions (in this case) are bimodal, and the differences between the distributions from the network and internetwork regions are evident. We see (in Fig. 2*a*) that the mean frequencies of the packets in the network is 3.74 mHz, while it is 5.06 mHz in the internetwork region, a difference that has been known for some time (e.g., Liu & Sheeley 1971). We can also see (Fig. 2*b*) that there are ~1.5 more packets in internetwork regions than there are in network regions over the duration of time series. The packets themselves are of very similar duration (Fig. 2*c*), with distribution means separated by only 1 minute in each region. This implies that there are a different number of individual oscillations ($\hat{P}_X$) within each packet in the network (~1.5 periods) and internetwork (~2.3 periods) regions. Likewise, in network regions, there are on average fewer packets that have a shorter duration, so the wait time between packets is longer, as demonstrated. Indeed, this is demonstrated in Figure 1*d*, where the mean network packet wait time is some 4 minutes longer. Physically speaking, the parameter distributions in this data set provide a valuable insight into the nature of chromospheric oscillations in what are assumed to be vastly different magnetic environments. The excess of packet suppression and the short coherence times (small number of periods per packet) in network regions are indicative of the apparent influence of the magnetic field on the oscillation's piston mechanism in the chromospheric network relative to that in the internetwork regions.

In Table 1 we present the details of the analysis of the eight *TRACE* 1700 Å continuum time series data sets. Each quantity

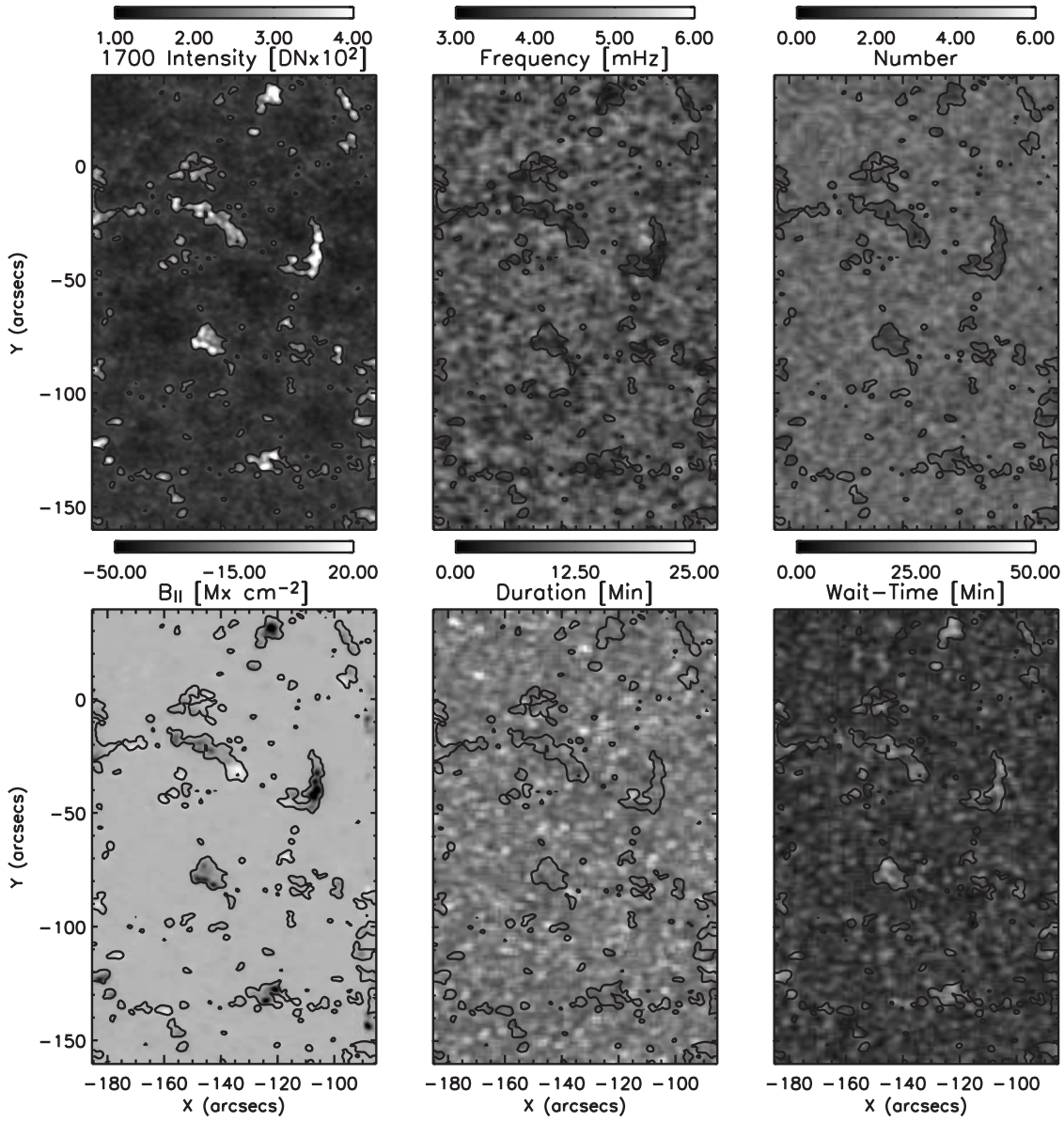

FIG. 4.—Spatial dependence of the *TRACE* packet parameters derived from the JOP 72 full FOV data of 1999 February 26 (4). In the center and right columns we demonstrate the spatial behavior of the packet parameters beside those of the mean *TRACE* 1700 Å continuum intensity (*top left*) and the MDI mean line-of-sight magnetic field strength $B_{\|}$ (*bottom left*). Many of the features discussed in the text and shown in Table 1 are clear. [*See the electronic edition of the Journal for a color version of this figure*.]

presented is the mean value of the distribution for that region at $1'' \times 1''$ spatial resolution, and each has a corresponding deviation, which for the purpose of limiting the size of this table are omitted.[6] We can see that some of the packet parameter variations have a dependence on the MDI unsigned network line-of-sight magnetic flux density B^* (units of Mx cm^{-2}). We see that the ν_X are typically lower in the network regions, $\sim$3.4 mHz, than in the internetwork regions, $\sim$4.0 mHz, but the values of ν_I appear to scale with B^*. We also see that the packet duration and wait time vary inversely (long duration, short wait time and vice versa). There are considerably more packets in the internetwork regions, and the number per hour ($\hat{N}_X$) is dependent on the mean field strength. Similarly, the number of peak-to-peak oscillations per packet is approximately uniform in the internetwork regions, at $\sim$2.5, while in the network regions it decreases from 2.5 in set 4 to 1.5 in set 7 as B^* increases; i.e., there are fewer pulses per packet in strong-network regions. This effective quenching of chromospheric oscillations and oscillatory power has been widely discussed, both by the present author in previous publications and in, for example, Title et al. (1992).

From top to bottom Figure 3 illustrates the dependence of the mean values (and variances) of ν_X, $\hat{N}_X$, D_X, Δt_X, and $\hat{P}_X$ with B^* of the network (*dark circles*) and internetwork (*light circles*) columns of Table 1 along with their respective least-squares linear fits and gradients (M_X). Figure 3*a* shows that ν_X in the network regions is invariant with B^* (within the error bars), while in internetwork regions, the value of

[6] We refer the reader to Table 2 and Fig. 3, which have typically representative values of the distribution deviation for each of the time series presented. Table 2 also shows values of the packet parameters for the other *TRACE* UV continuum bandpasses.

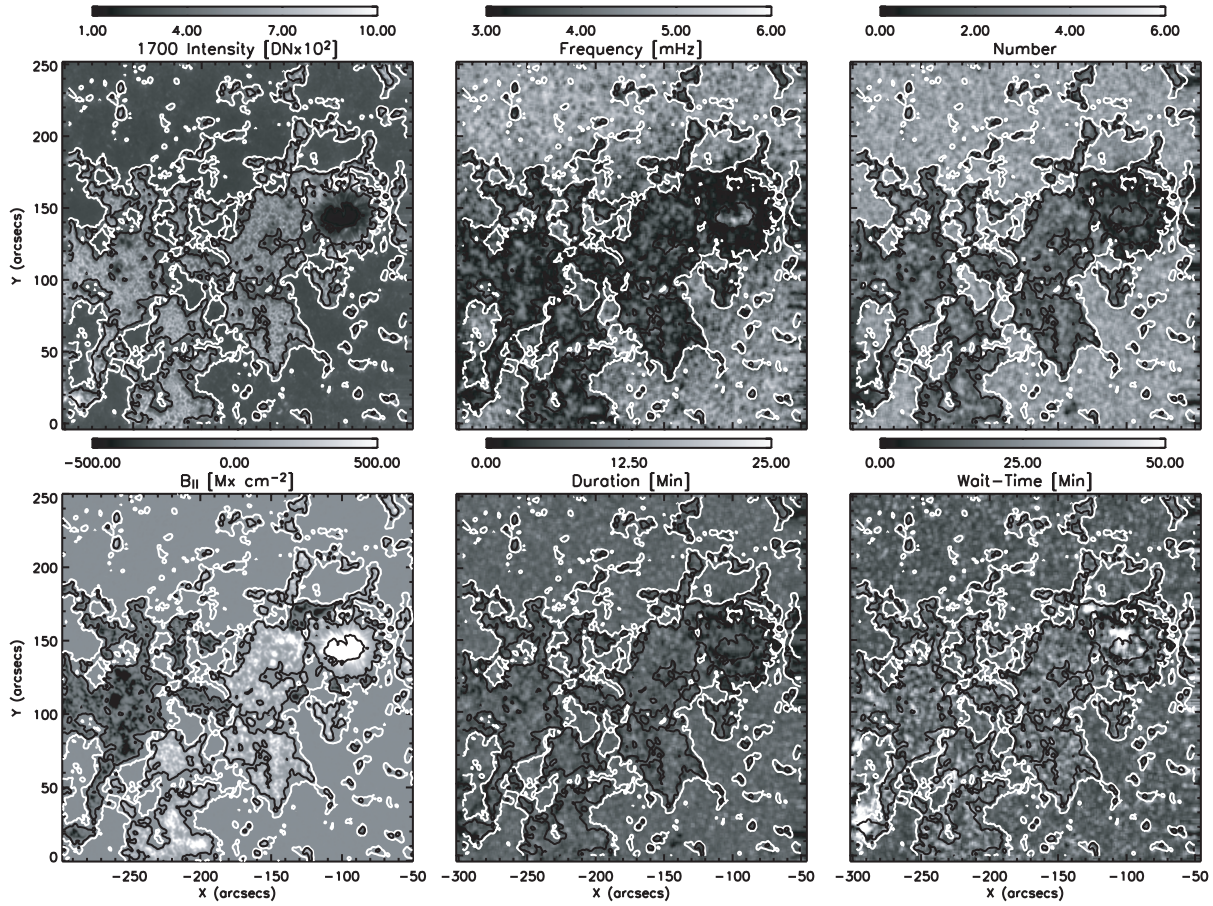

FIG. 5.—Spatial dependence of the *TRACE* packet parameters derived from the JOP 97 full FOV data of 2000 September 22 (7). See Fig. 4 for panel details. [*See the electronic edition of the Journal for a color version of this figure.*]

ν_X shows a small increase, although we note that the use of a linear fit in this case is probably inaccurate because most of the growth occurs from $B^* \geq 75$ Mx cm^{-2}. The growth of ν_I as B^* increases is indicative of a contamination of internetwork structure by the lowering and expansion of the chromospheric "canopy," and we discuss this further below. In Figures 3*b* and 3*c* we see that the linear fits to $\hat{N}_X$ and D_X are effectively parallel to one another. In both cases this suggests that the degree by which the packet generation mechanism is suppressed or truncated increases with B^*, no matter what region we are considering. This, again, points to the influence of the network magnetic field strength and its expanding outward topology on the internetwork regions. In Figure 3*d* it is clear that the network wait time does not vary with B^*. Hence, the separation between oscillations is independent of B^* inside network elements. However, the internetwork wait times increase with B^*, which is consistent with the decreasing packet durations and, from Figure 3*e*, the fact that the number of periods per packet is effectively invariant. Likewise, in Figure 3*e*, we suggest that the decrease in network periods per packet with B^* is due to the invariant wait time of Figure 3*d* and the decreasing packet durations of Figure 3*c*.

The details and relationships of the packet parameters presented in Table 1 and Figure 3 point to global *p*-mode interference as the local piston responsible for the chromospheric oscillation packets observed. The decrease in the number of packets, the anticorrelated variations in packet duration and wait time (particularly in internetwork regions), and all of the parameters' variations with B^* point to a degree of systematic regularity in the piston responsible, irrespective of where they are observed.

4.1. *Spatial Behavior*

We explore the spatial distributions of the packet parameters to expand upon some of the relationships discussed above. As examples we use data sets from the opposite ends of the topographic spectrum, the "weak-field" case of 1999 February 26 (set 4) in Figure 4 and again, the sunspot, "strong-field" case of 2000 September 22 (set 7) in Figure 5.

In the center and right columns of Figures 4 and 5, we demonstrate the spatial behavior of the packet parameters beside those of the mean *TRACE* 1700 Å continuum intensity (*top left*) and MDI $B_{\|}$ (*bottom left*). The solid black contour shown on each panel marks the boundary between the network and internetwork plasma as defined above. Several features are immediately clear, as we might expect from the discussion above. The lower packet frequencies inside the network regions are contained within these contours (*top middle*). Similarly, in network regions, there appear to be fewer packets (*top right*), which is consistent with the fact that the wait time is significantly longer there (*bottom right*). Despite all of these relatively strong spatial correlations, the packet duration (*bottom middle*) shows little dependence on where the packets are located. On comparing the packet frequency panels we can clearly see, as was noted above, that the internetwork frequencies in set 7 ($\sim$5.1 mHz) are significantly different from those in set 4 ($\sim$4.0 mHz), which could very much be considered as a typical "quiet" internetwork oscillation

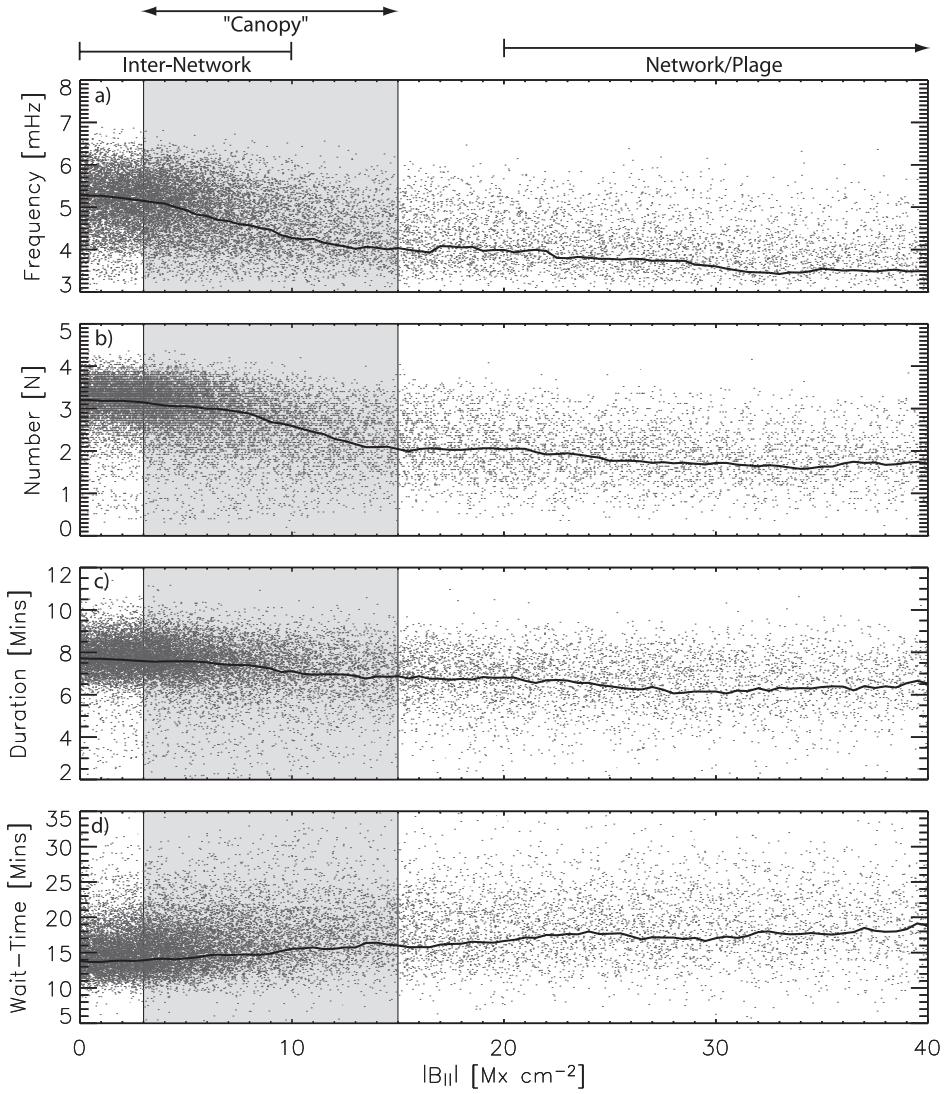

FIG. 6.—Scatter plots showing the variations of the four packet parameters as a function of the $|B_{\|}|$ for the JOP 97 sunspot data of 2000 September 22 (7) of Figs. 2 and 5. We can clearly see the origin of the bimodal packet parameter distributions in the separation of the internetwork and network values. The transition of the packet parameters between these defined regions points to the influence of the intermediate magnetic region or magnetic canopy (*gray shaded region*).

frequency in the *TRACE* 1700 Å bandpass. Indeed, we can also see in Figure 5 that there is a relatively smooth transition from network to internetwork frequencies that is indicative of the canopy effects on chromospheric oscillations that were demonstrated in the figures of Krijger et al. (2001) and McIntosh & Judge (2001).

From Figure 5 it is clear that there is a broad enough range of magnetic flux densities to quantitatively explore the broad, bimodal, all-pixel parameter distributions shown in Figure 2 and the influence of the extended magnetic canopy on the packet parameters. Figure 6 shows scatter plots of packet frequency (Fig. 6*a*), number (Fig. 6*b*), duration (Fig. 6*c*), and wait time (Fig. 6*d*) versus the corresponding (co-aligned) absolute values of $B_{\|}$ ranging from 0 to 40 Mx cm^{-2}. In each panel, the solid line corresponds to the location of the maximum scatter density at each value of $|B_{\|}|$ and can clearly see that there is a smooth transition from the true internetwork[7] to the effectively constant network values at about 20 Mx cm^{-2}. The gray shaded regions of smooth transition can be attributed to the magnetic canopy.

4.2. *Multiwavelength Wave Packet Analysis*

In addition to providing *TRACE* (1700, 1600, and 1550 Å) time series observations of a (very) quiet region near disk center, data set 4 has complementary *SOHO* MDI (Doppler velocity; $V_{\|}$) and Solar Ultraviolet Measurements of Emitted Radiation (SUMER; Wilhelm et al. 1995: 1195 Å continuum, N I $\lambda\lambda$1199.55 and 1200.22, Si II λ1197.40, and Si III λ1206.51) time series observations, allowing us to analyze the wave packet parameters over a large vertical extent, effectively "tracking" their average behavior from the photosphere through the chromosphere and into the transition region plasma with the gradual decay of the internetwork magnetic field.[8]

[7] At this stage we should note that our defined internetwork magnetic field bounds are generous; we should ideally have $|B_{\|}| \sim 0$ Mx cm^{-2}. Because we use too broad a range in $B_{\|}$, the distributions of internetwork parameters are artificially wide in some cases (e.g., set 7).

[8] Similar analyses of such data sets have been made but were restricted to sunspot umbrae or individual strong-network elements (see, e.g., O'Shea et al. 2002; McAteer, Gallagher, & Williams 2003).

TABLE 2

INTERNETWORK PACKET DETAILS FROM THE COMBINED ANALYSIS OF THE JOP 72 *SOHO* MDI/SUMER AND *TRACE* OBSERVATIONS OF 1999 FEBRUARY 26 (SET 4)

Observable	z (Mm)	$\hat{N}_I$	ν_I	D_I	Δt_I	$\hat{P}_I$
MDI $V_\parallel$	0.2	2.41 ± 0.43	3.38 ± 0.16	12.87 ± 3.01	11.78 ± 4.12	2.61 ± 0.44
TRACE 1700 Å	0.3–0.6	2.36 ± 0.37	3.99 ± 0.28	12.08 ± 2.25	12.69 ± 4.15	2.89 ± 0.29
TRACE 1600 Å	0.3–0.6	2.36 ± 0.37	4.07 ± 0.31	11.80 ± 2.17	12.40 ± 3.92	2.88 ± 0.28
TRACE 1550 Å	0.3–0.6	2.34 ± 0.67	4.08 ± 0.31	11.77 ± 2.22	12.51 ± 3.98	2.88 ± 0.31
SUMER continuum	0.7–1.0	2.36 ± 0.42	4.37 ± 0.92	10.01 ± 3.08	12.45 ± 5.91	2.43 ± 0.39
SUMER V N I 1199.55 Å	≥1.0	2.50 ± 0.52	4.36 ± 1.07	8.83 ± 5.29	12.20 ± 5.16	2.44 ± 0.41
SUMER V N I 1200.22 Å	≥1.0	2.53 ± 0.56	4.38 ± 1.05	8.87 ± 5.20	12.29 ± 5.24	2.43 ± 0.32
SUMER V Si II 1197.40 Å	≥1.50	2.54 ± 0.92	4.64 ± 1.30	8.22 ± 3.27	11.58 ± 5.90	2.36 ± 0.36
SUMER V Si III 1206.51 Å	≥1.75	2.69 ± 0.83	4.87 ± 0.78	7.75 ± 2.62	11.87 ± 6.24	2.26 ± 0.42

NOTE.—We identify the observable, an estimate of where the signal is formed, the four internetwork packet parameters, the number of periods per packet, and their associated errors (derived as standard deviations of the distributions).

The raw SUMER data have been spatially rescaled to two-pixel ($2'' \times 1''$, along the slit) blocks to more accurately describe the spatial distribution of the packets and improve the signal-to-noise ratio. This rebinning is below the SUMER spatial correlation length scale of $5''$ that was derived by Judge et al. (2001). During these observations the *SOHO* spacecraft was rolled at $119^\circ.2$ to the solar north-south line (see Fig. 1 of Judge et al. 2001), and so SUMER was not correcting its observations for solar rotation; as a result, the SUMER spectroscopic data drift spatially, but steadily, by several arcseconds ($<10''$) over the duration of the observations. We have not attempted to remove the effects of solar rotation drift in the SUMER time series to avoid introducing additional frequency-dependent noise in our calculations.

In Table 2 and Figure 7 we present the results of applying the Morlet wavelet analysis discussed above to the internetwork data of data set 4.[9] The packet frequencies (ν_I; in Fig. 7*a*) show a gradual increase with height, and therefore the period decreases from approximately 5 minutes for the MDI $V_\parallel$ data to approximately 3.5 minutes in the Si III line and is consistent with the results of Judge et al. (2001). The number of packets per hour ($\hat{N}_I$; Fig. 7*b*) increases very slightly, but not significantly, within the error bars, and is consistent with the weak dependence on $B_\parallel$ that was observed in Table 1 and Figure 3. Given those results, we would expect that the packet frequency increase with height implies a decrease in the packet duration (D_I) *if* the number of internetwork periods per packet ($\hat{P}_I$) is unchanged, as shown in Figures 7*c* and 7*e*, respectively. The wait times (Δt_I; Fig. 7*d*) do not correspond, as expected, with the D_I because, as the packets become shorter, the time between packets must increase *if* $\hat{N}_I$ is unchanged. In fact, little variation in wait time is observed, which is possibly a result of the increase in $\hat{N}_I$ being real or an underestimation, as discussed in § 3, but we note that there are large error bars associated with the wait times.

In general, there are significantly larger errors associated with the packet parameters derived from the SUMER lines than with those from the MDI or *TRACE* time series, mostly because of the high noise content of the SUMER data and the small number of pixels available to sample (we have used the internetwork regions of the entire *TRACE* MDI FOV). The effects of a high noise level could include "washing out" of oscillations in true wave packets, or conversely, sections of noise could be mistaken for true oscillations. In both cases we expect a reduction in duration (e.g., observing a lengthy "noise packet" is unlikely; O'Shea et al. 2002), while these combined effects could also explain the slight increase in packet number observed. This increase in packet number will, to some extent, cancel out the effect of reduced duration on the wait times, which may explain their apparent lack of variation.

Clearly, the packet parameters show variations with height, but they require further investigation. One interesting relationship, if real, is the apparent increase of $\hat{N}_I$ and whether it means that additional packets are being "created" in the low-β transition region plasma, i.e., if the oscillation itself acts as a piston or if observable packets are "converted" from nonobservable packets in the magnetic canopy (cf. Bogdan et al. 2003). Therefore, it will be useful to obtain and analyze more data sets for which SUMER (or higher spatial resolution transition region spectroscopic) observations are coordinated with those of *TRACE* and MDI to understand the vertical relationships of the wave packet parameters accurately.

5. FUTURE CONSIDERATIONS

Several of the features discussed above require some further investigation that is beyond both the quality of the data presented and the scope of this paper. By far the most important of these is the potential to isolate, quantify, understand, and actually connect the observed chromospheric oscillations to the piston that generates them (see also Cadavid et al. 2003; Lawrence et al. 2003). Much of the data available today, including those presented here, are of insufficient spatial resolution to address the connection of oscillation and generator, but the method detailed is very applicable to the task of looking for local wave and propagation (refraction, reflection and conversion) effects. By studying wave packets in the Earth's oceans, Liu (2000) has constructed simple cross-wavelet correlation, coherence, and phase difference relationships that may help us understand the piston mechanism better.

Other questions exist. What role does wave-mode interference play in the magnetic canopy in dictating what we observe there? The simulations of Rosenthal et al. (2002) and Bogdan

[9] Observe that each of the packet parameters for the 1550, 1600, and 1700 Å *TRACE* UV continua (Fig. 7, *black circle*) give extremely close and consistent values, as may have anticipated, given that their formation regions are not significantly separated.

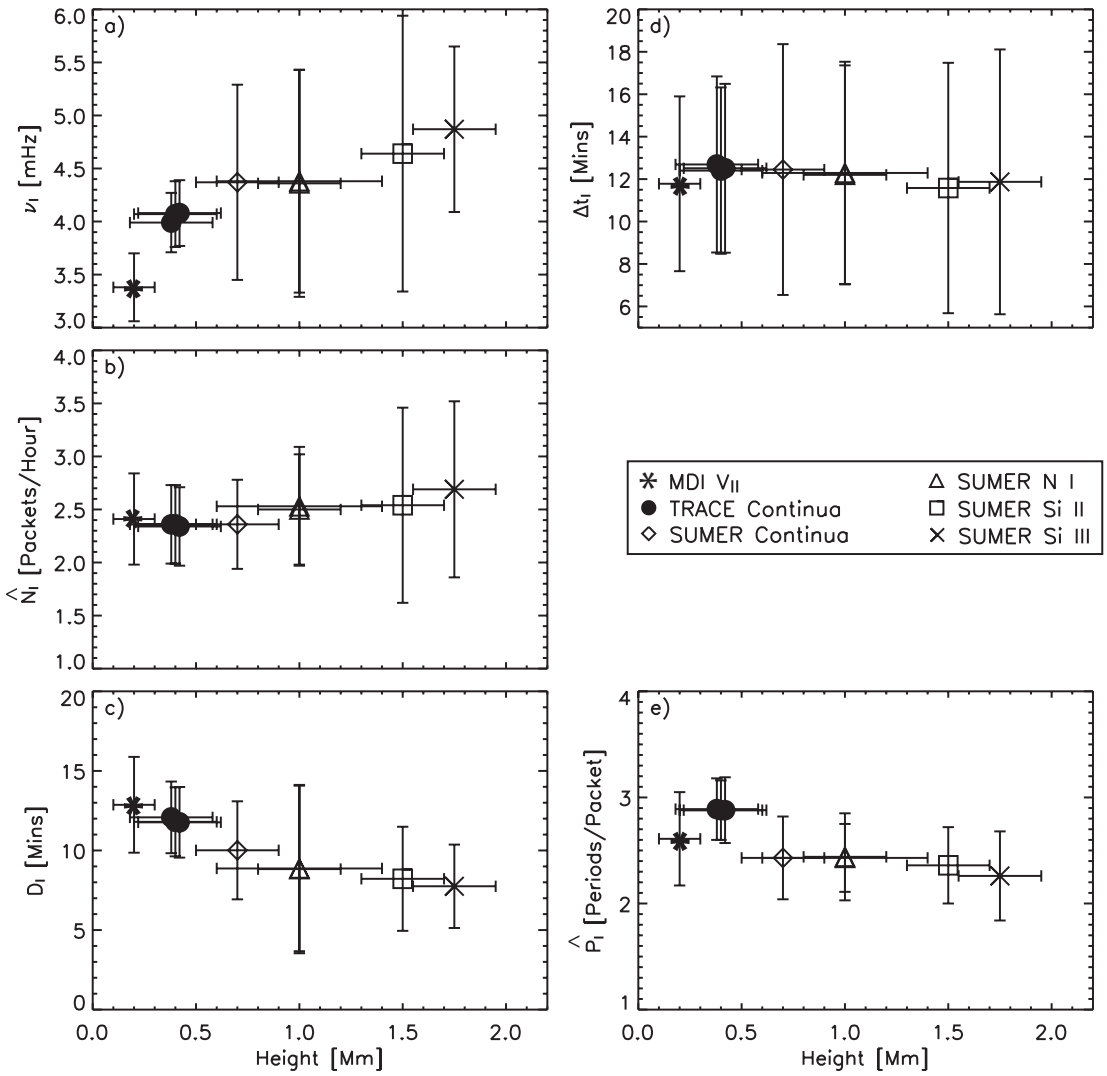

FIG. 7.—(*a*) Packet frequency, ν_I, (*b*) number of packets per hour, $\hat{N}_I$, (*c*) packet duration, D_I, (*d*) wait time, Δt_I, and (*e*) number of oscillation periods per packet $\hat{P}_I$, and their variation with the assumed formation "height" of the observable for the JOP 72 data of 1999 February 26 (4).

et al. (2002, 2003) demonstrated the canopy as a realm where magnetoatmospheric wave modes of different frequencies and magnetic influences can impinge and beat on one another readily. Similarly, the suppression of packet number, short packet duration, and oscillatory power by strong-network, or plage, magnetic fields has been noticed, and again we ask what role the plasma topography plays in this phenomenon. Is this a situation in which interference is important again, where short, quasi-periodic pulses of constructive interference "mislead" the wavelet analysis, or is the plage region a tangled mess of low-lying, high–pitch-angle field structures that suppress wave modes (see observational and simulation examples in McIntosh et al. 2001, McIntosh & Judge 2001, and Rosenthal et al. 2002)?

We plan to acquire high-cadence "synoptic" observations in the 1700 and 1600 Å UV continua at a fixed high cadence (of the order of 10 s) to build a catalog of different solar topographies for comprehensive study of wave packets as well as other spatial and spectral phenomena as a first step.

6. DISCUSSION

In the preceding sections, we have seen that chromospheric oscillations are not persistent in time, but last on average only a few periods before dying out, only to reappear some time later. These short-duration bursts of oscillation are clearly identifiable as being multifrequency packets in the time series observations. The localization of the packets in frequency and time makes their analysis readily amenable to wavelet transforms. We have seen that the characteristic scales of oscillation intermittence are tied to the magnetic environment in which they are generated (through either granular collapse or global *p*-mode interference). In an effort to understand and quantify these ties, we have parameterized the occurrence of chromospheric oscillation wave packets through their mean frequency, duration, number, and wait time. In § 4 we have explored the statistical and spatial behavior of the wave packet parameters and demonstrated their dependence and variation with one another and with the magnetic topology that threads the chromospheric plasma.

We show in Figure 8 qualitative (idealized axisymmetric) cartoon visualizations of the plasma topography in the strong- and weak-field cases for comparison with those presented in Figures 4 and 5 and with their two-dimensional counterparts presented in Gabriel (1976). This figure is meant to explain the role of the plasma topography in dictating the wave packet frequency and subsequently the other wave

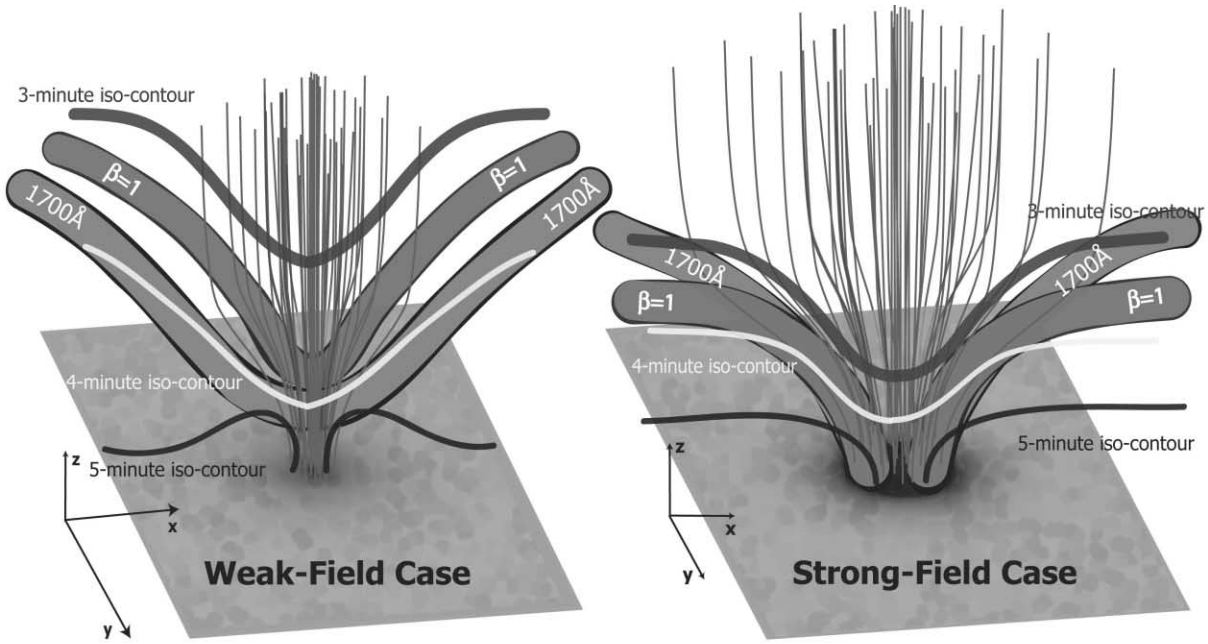

FIG. 8.—Cartoon visualizations of the plasma topography in the strong- and weak-field cases. In each visualization we show the field topology (*thin gray solid lines*), the plasma-$\beta = 1$ isocontour (*thick band labeled* $\beta = 1$), an estimate of the vertical position of the *TRACE* 1700 Å continuum formation layer (*thick band labeled 1700* Å), and the planar total (gas+magnetic) pressure isobars, which correspond to the topographic locations where 5 minute (*solid thick black line*), 4 minute (*solid thick light* line), and 3 minute (*solid thick gray line*) period waves form the characteristic period of oscillation. [*See the electronic edition of the Journal for a color version of this figure.*]

packet parameters. The spatial (*x*-*y*) scales of each cartoon are different, with the weak-field case (*left*; 1 Mm) having twice the spatial scale of the strong-field case (*right*; 10 Mm). We assume that the vertical (*z*) scales are the same (1 Mm). In each cartoon we show a representative magnetic field topology (*thin gray solid lines*), a plasma-$\beta = 1$ isocontour (*thick gray band*), an estimate of the vertical position of the *TRACE* 1700 Å continuum formation layer (*thick band*), and the total atmospheric pressure (gas pressure plus magnetic pressure) isobars that correspond to the topographic locations where 5 minute (3.3 mHz; *solid thick black line*), 4 minute (4.2 mHz; *solid thick line*), and 3 minute (5.6 mHz; *solid thick line*) period waves are predominant. Notice the topological differences in each cartoon, the differing horizontal spread of the field, and the net effect that the strength of the magnetic field has in contributing to the lowering of the characteristic period isosurfaces and the plasma-$\beta = 1$ isocontour, i.e., the magnetic canopy, into the internetwork regions.

We propose that the intersection of the TRACE 1700 Å *formation surface and the characteristic period isosurfaces determines the frequency of wave packets that are observed and can explain some of the features observed in the figures and tables of this paper.* Again, we use the internetwork regions of sets 4 and 7 as examples to illustrate this proposition. Typical chromospheric oscillations present in *TRACE* 1700 Å bandpass time series of the internetwork have a 4 minute period; compare this to left side of Figure 8, where the formation surface samples the 4 minute pressure isocontour just outside out of the network element core and out into the internetwork region. In Figure 5, however, we see that the internetwork frequencies were approaching those of 3 minute waves, but we would expect to find 3 minute waves at significantly higher levels of the typical internetwork atmosphere, say at SUMER continuum levels like those discussed by McIntosh et al. (2001). It would appear that the atmosphere "shrink-wraps" itself around the network elements, thus significantly altering the total pressure structure of the atmosphere around the magnetic element. How far that influence is carried is determined by the strength of the magnetic field in the network elements: the stronger the flux, the more far-reaching its effect on the internetwork plasma.

Through the combined analysis of *TRACE*, SUMER, and MDI time series data, we have demonstrated that these characteristic wave packet parameters are consistent with current pictures of wave interaction with the chromospheric canopy. The connection of wave packet parameters and the underlying magnetic field makes this technique into a basic structural diagnostic of the chromospheric plasma. Further, the timing and spatial structure of the wave packet parameters point to global *p*-mode interference as the chromospheric oscillation wave packet generation mechanism in the lower regions of the atmosphere, although this, for the reasons mentioned above, must be investigated further.

The authors would like to thank Rob Rutten for taking the time to help us greatly improve the content and clarity of this paper. D. G. S. acknowledges the support of the NASA GSFC/LASP summer intern program. S. W. M. acknowledges the support of the GSFC SDAC and NASA's Living With A Star program and would also like to thank Professor John Lawrence and Alex Young for discussions on wavelet transform applications. Finally, we thank the *TRACE* instrument team for making their data available and agreeing to conduct a synoptic 1600/1700 Å observation program.

REFERENCES

Bogdan, T. J., et al. 2002, Astron. Nachr., 323, 196
———. 2003, ApJ, 599, 626
Cadavid, A. C., Lawrence, J. K., Berger, T. E., & Ruzmaikin, A. 2003, ApJ, 586, 1409
Cha, M. Y., & White, O. R. 1973, Sol. Phys., 31, 55
Deubner, F.-L., & Fleck, B. 1990, A&A, 228, 506
Fleck, B., Domingo, V., & Poland, A. I., ed. 1995, The *SOHO* Mission (Dordrecht: Kluwer)
Gabriel, A. H. 1976, Philos. Trans. R. Soc. London A, 281, 339
Handy, B. N., et al. 1999, Sol. Phys., 187, 229
Judge, P. G., Tarbell, T. D., & Wilhelm, K. 2001, ApJ, 554, 424
Krijger, J. M., et al. 2001, A&A, 379, 1052
Lawrence, J. K., et al. 2003, ApJ, 597, 1178
Lites, B. W., Chipman, E. G., & White, O. R. 1982, ApJ, 253, 367
Liu, P. C. 2000, in Advances in Coastal and Ocean Engineering, Vol. 6, ed. P. L. F. Liu (Singapore: World Scientific), 57
Liu, S. Y., & Sheeley, N. R. 1971, Sol. Phys., 20, 282
McAteer, R. T. J., Gallagher, P. T., & Williams, D. R. 2003, ApJ, 587, 806
McIntosh, S. W., Fleck, B., & Judge, P. G. 2003, A&A, 405, 769
McIntosh, S. W., & Judge, P. G. 2001, ApJ, 561, 420
McIntosh, S. W., et al. 2001, ApJ, 548, L237
Muglach, K., & Hofmann, A. 2003, A&A, submitted
O'Shea, E., Muglach, K., & Fleck, B. 2002, A&A, 387, 642
Rast, M. P. 1999, ApJ, 524, 462
Rhodes, E. J., Ulrich, R. K., & Deubner, F.-L. 1979, ApJ, 227, 629
Rosenthal, C. S., et al. 2002, ApJ, 564, 508
Rutten, R. J. 2003, in Proc. NATO Advanced Research Workshop on Turbulence, Waves, and Instabilities in the Solar Plasma, ed. R. Erdélyi, K. Petrovay, B. Roberts, & M. J. Aschwanden (Dordrecht: Kluwer)
Scherrer, P. H., et al. 1995, Sol. Phys., 162, 129
Skartlien, R., & Rast, M. P. 2000, ApJ, 535, 464
Title, A. M., Topka, K. P., Tarbell, T. D., Schmidt, W., Balke, C., & Scharmer, G. 1992, ApJ, 393, 782
Torrence, C., & Compo, G. P. 1998, BAAS, 79, 61
Ulrich, R. K. 1970, ApJ, 162, 993
White, O. R., & Cha, M. Y. 1973, Sol. Phys., 31, 23
Wilhelm, K., et al. 1995, Sol. Phys., 162, 189